

Experiments on plasma detachment in a V-shaped slot divertor in the DIII-D tokamak

R. Maurizio^{1,*} , D. Thomas¹ , J.H. Yu¹ , T. Abrams¹ , A.W. Hyatt¹ , J. Herfindal² ,
A. Leonard¹ , X. Ma¹ , A.G. McLean³ , J. Ren⁴ , F. Scotti³ , M.W. Shafer² ,
G. Sinclair¹ , H.Q. Wang¹  and J. Watkins⁵

¹ General Atomics, San Diego, CA 92186, United States of America

² Oak Ridge National Laboratory, Oak Ridge, TN 37831, United States of America

³ Lawrence Livermore National Laboratory, Livermore, CA 94550, United States of America

⁴ University of Tennessee Knoxville, Knoxville, TN 37996, United States of America

⁵ Sandia National Laboratory, Albuquerque, NM 87185, United States of America

E-mail: maurizior@fusion.gat.com

Received 15 January 2024, revised 24 May 2024

Accepted for publication 17 June 2024

Published 3 July 2024



Abstract

Experiments in DIII-D demonstrate that the upstream plasma density to detach an un-pumped slot divertor is similar for a V-shaped and a flat-end slot, despite significantly higher neutral pressure in the V-shaped slot and in contrast to SOLPS-ITER predictions. The detachment threshold can be reduced by using in-slot instead of main-chamber gas fuelling or by placing the strike point on the inner slanted slot baffle instead of the slot end, as described by simulations with full drift physics. When increasing the plasma line-averaged density (without extrinsic impurities), the transition to detachment in DIII-D slot divertor is sharp and requires a high value of plasma density with the ion $\vec{B} \times \nabla B$ drift into the slot, whereas it is smooth and requires a lower value of plasma density with the opposite drift direction, in accord with detachment experiments in the DIII-D open lower divertor. Unique experiments on DIII-D and comparison to advanced simulations expand the scientific understanding of slot-shaped divertors, considered highly desirable for next step fusion devices.

Keywords: power exhaust, divertor, DIII-D, FEC 2023, slot divertor, detachment

(Some figures may appear in colour only in the online journal)

1. Introduction

A key outstanding issue for the development of steady-state nuclear fusion power plants is the design of divertor structures able to safely withstand the projected plasma power

and particle exhaust fluxes. Due to physical limitations on the divertor target heat load and plasma temperature at the divertor plate [1, 2], the majority of the exhausted plasma energy, momentum and particle flows have to be mitigated in the divertor volume, i.e. after leaving the confined plasma core but before reaching the divertor plates along field lines. Numerous experiments across different tokamak devices, including DIII-D, have shown that the achievement of such highly dissipative (detached) divertor conditions without negatively affecting the confined plasma conditions is very challenging [3–7].

A route for divertor design optimization is to increase the closure of divertor structures around the location where

* Author to whom any correspondence should be addressed.



Original content from this work may be used under the terms of the [Creative Commons Attribution 4.0 licence](https://creativecommons.org/licenses/by/4.0/). Any further distribution of this work must maintain attribution to the author(s) and the title of the work, journal citation and DOI.

the plasma exhaust power fluxes hit the divertor plate. This approach is designed to increase the retention of recycled neutral atoms inside the divertor volume, densifying and thus cooling the plasma (volumetric radiation is proportional to plasma density) when compared to open divertor configurations, where neutrals are able to transport up to the main chamber (MC) in the scrape-off layer (SOL). Over several decades, numerous experiments have pursued this strategy [8], with recent examples including the TCV and MAST-U tokamaks. At TCV, the installation of removable divertor gas baffles effectively divided the vessel into separate divertor and MCs. This setup resulted in a colder and denser divertor plasma, allowing access to detached conditions at lower upstream plasma densities compared to unbaffled cases [9]. Similarly, upgrades at the MAST-U tokamak aimed to investigate detachment in configurations with very elongated outer divertor legs, known as the Super-X. In this configuration, strong wall baffling surround the majority of the outer leg, effectively creating a divertor chamber separate from the MC [10].

An extreme degree of closure is achieved in slot-shaped divertors which, as a result, are considered to be potentially highly desirable for next step fusion devices. However, actual well-diagnosed experimental data on their exhaust behaviour compared to more conventional divertor shapes is limited.

To expand the scientific understanding of slot divertors, and determine their scalability to a fusion power plant, the DIII-D tokamak (San Diego, CA, USA) research program promoted the design, installation and testing of two subsequent slot divertor concepts.

The first concept, known as the small-angle slot divertor (SAS), was designed using the SOLPS-ITER code in 2016–2017 and installed and tested in 2018–2021, see figure 1(a). Experiments found power exhaust benefits of SAS compared to less closed divertor concepts in terms of lower plasma density required to reach highly dissipative conditions in the outer divertor, but only in the case where the ion $\vec{B} \times \nabla B$ direction is directed out of the divertor [11]. Remarkably, the benefits for detachment onset were found to be negligible for the opposite field direction compared to the open divertor case. Extensive subsequent simulations incorporating a full drift physics model also reproduced these results and explained the closure benefit as due to both improved recycled neutral retention and beneficial changes in the particle drift 2D flow patterns [12, 13].

The second slot concept, known as the V-shape small angle slot (SAS-VW), was again designed with SOLPS-ITER in 2020 and installed and tested from 2022 onwards, see figure 1(b). This modified version of SAS features a V-shape slot end instead of a flat end. Additionally, the outer (outboard) row of carbon tiles is coated with a thin layer of tungsten to study W sourcing, leakage and SOL accumulation [14]. The influence of the tungsten coating on the detachment physics of the main deuterium and carbon (D + C) plasma is expected to be minor for several reasons: (1) near detachment onset, when the electron temperature at the target is below 10 eV, minimal tungsten erosion occurs (the W sputtering threshold

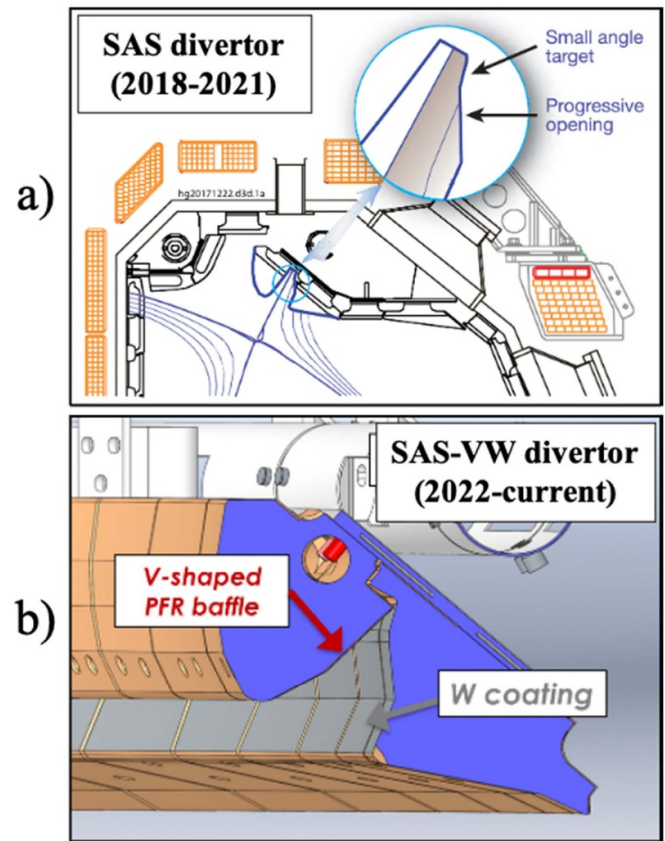


Figure 1. (a) Schematic of the SAS divertor, Reproduced from [11]. © 2019 IAEA, Vienna. All rights reserved, and (b) of the SAS-VW divertor, Reproduced from [14]. © IOP Publishing Ltd. All rights reserved.

is approximately 50 eV for carbon and 200 eV for deuterium [15]), resulting in no significant tungsten source; (2) while the overall carbon source might experience a reduction due to the tungsten coating, this impact is expected to be minor compared to the integrated carbon source from the remaining divertor and MC walls; and (3) furthermore, the deuterium recycling efficiency is very similar on both carbon and tungsten surfaces. Hence, tungsten's presence was not included in the modelling, and the slot is denoted as 'SAS-V' in the modelling but 'SAS-VW' in the experiment. For an in-depth analysis of the tungsten measurements from the same SAS-VW campaign, refer to [16–18].

Initial SOLPS-ITER modelling from [19] indicated that SAS-V reduced target electron temperature compared to SAS, acting in a much more symmetric way for both ion $\vec{B} \times \nabla B$ drift directions, unlike SAS. Consequently, SAS-V was expected to achieve lower target temperatures than a matched open divertor configuration for both field directions, unlike SAS. The first modelling effort of SAS-V used a set of simplifications to facilitate convergence and accelerate the modelling process. Higher fidelity simulations of SAS-V [20] assessed the slot behaviour without many of the above-mentioned approximations, and still found that the electron temperature near the strike point is reduced in SAS-V compared to SAS, for

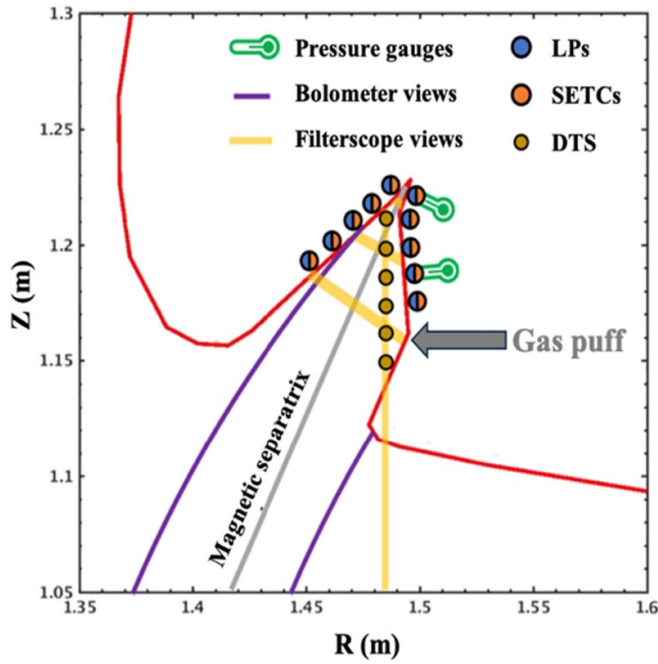


Figure 2. Sketch of the SAS-VW divertor, showing key diagnostics: Langmuir probes (LPs, in blue), surface eroding thermocouples (SETCs, in orange), divertor Thomson scattering (DTS, in brown), ASDEX-style pressure gauges (green), bolometer views (violet) and filterscope views (yellow). The poloidal location of the in-slot gas puff is shown, while the main chamber gas puff location is at $R = 1.94$ m outside of the divertor region.

all simulated densities ($n_{e,sep}$ from ~ 0.5 to $\sim 2 \times 10^{19} \text{ m}^{-3}$), heating powers (4 and 8 MW) and for both magnetic field directions.

This paper presents DIII-D experiments characterising the power exhaust performance of SAS-VW, for H-mode plasmas in the USN configuration and with the outer strike point placed inside the V-shaped slot, with 4–5 MW of heating power and plasma current of 1 MA. The transition from attached divertor conditions (low radiation, high target plasma temperature, $T_e > 20$ eV) to detached divertor conditions (significant volumetric radiation, low target plasma temperature, $T_e < 5$ eV) is achieved by gradually increasing the core plasma density via increased deuterium fuelling rate (using a gas valve located in the MC or one injecting from inside the slot, at a single toroidal angle). The onset of divertor detachment is defined as when the ion saturation current in the near-SOL ($\psi_n = 1.007$) rolls-over as a function of the plasma line-average density.

The SAS-VW divertor features an extensive set of diagnostics to characterize local plasma conditions in detail, see figure 2. These include an array of Langmuir probes for target electron temperature and ion saturation current, an array of surface eroding thermocouples for target heat flux, two ASDEX-style pressure gauges for target neutral pressure (in the near and far-SOL), Divertor Thomson Scattering for electron density and temperature in the slot volume, bolometric views for volumetric radiated power and filterscope views for deuterium and tungsten lines' emission intensity. In addition, a tangential imaging system provides poloidal reconstructions

of the C-III line emission measurements of the slot divertor region including the X-point.

Divertor detachment onset in SAS-VW is studied as a function of slot shape (section 2, comparing SAS to SAS-V), position of fuelling valve (section 3), position of magnetic strike point (section 4) and magnetic drift direction (section 5). Section 6 presents some discussions of the results and conclusions.

2. Impact of slot shape on detachment onset

After the installation of SAS-VW, a series of matched dissipation experiments were conducted, replicating the approach adopted with the SAS divertor. Detachment onset is found to occur at essentially the same upstream plasma density in the SAS-VW divertor (figure 3(a)) as the legacy flat-end SAS (figure 3(b)), in each B_T direction (figure 3(d) for ion $\vec{B} \times \nabla B$ drift into the slot, figure 4(d) for ion $\vec{B} \times \nabla B$ out of the slot), despite significantly higher neutral pressure (figures 3(c) and 4(c)), neutral compression (ratio of near-SOL and far-SOL measurement) and particle fluxes (figures 3(f) and 4(f)) in SAS-VW compared to SAS. This also is in contrast to SOLPS-ITER modelling with full drifts (figure 3(e)), predicting that SAS-VW would enhance neutral pressure in the slot that, in turn, would flatten the target T_e profile in a way that reduces the $\vec{E} \times \vec{B}$ force responsible for transporting ions from the slot to the inner target, thus enabling detachment at low upstream plasma density [20]. DIII-D experiments clearly observe the predicted enhanced neutral pressure in SAS-VW relative to SAS, but see no change to the target T_e profile (figure 3(f)) and, consistently, no change to the line-averaged density required for detachment onset relative to SAS (figure 3(d)).

The original $\sim 10\%$ detachment density reduction of SAS-V compared to SAS predicted by SOLPS-ITER (figure 3(e) [20]) is therefore not experimentally observed. This is possibly because the uncertainty (scatter) in the measurements of target T_e could be comparable to the predicted difference between SAS and SAS-V (figure 3(e)). SOLPS-ITER predicts a relatively small difference in detachment behaviours between SAS and SAS-V, so it is reasonable to hypothesize that it could be too small to be measurable. Notable sources of uncertainty (scatter) for the measured T_e are the ELM-filtering procedure (low-pass filter), the errors involved in fitting the characteristic $I-V$ curve for each Langmuir probe and the uncertainty in the magnetic reconstruction of the strike point position. Additionally, the SAS-VW inboards tiles are slightly misaligned with respect to the magnetic axis at some toroidal locations because of mounting challenges (these tiles were attached to the conical plate supporting structure using the existing nut bars which allow for a limited degree of radial adjustments). This may also have contributed to the disagreement between modelling and experiment as tile misalignments can create 3D dynamics that are not captured by 2D boundary codes. However, experimental cross-checks with new and previous SAS results were conducted and it was concluded that the misalignment impacts are likely to be marginal for

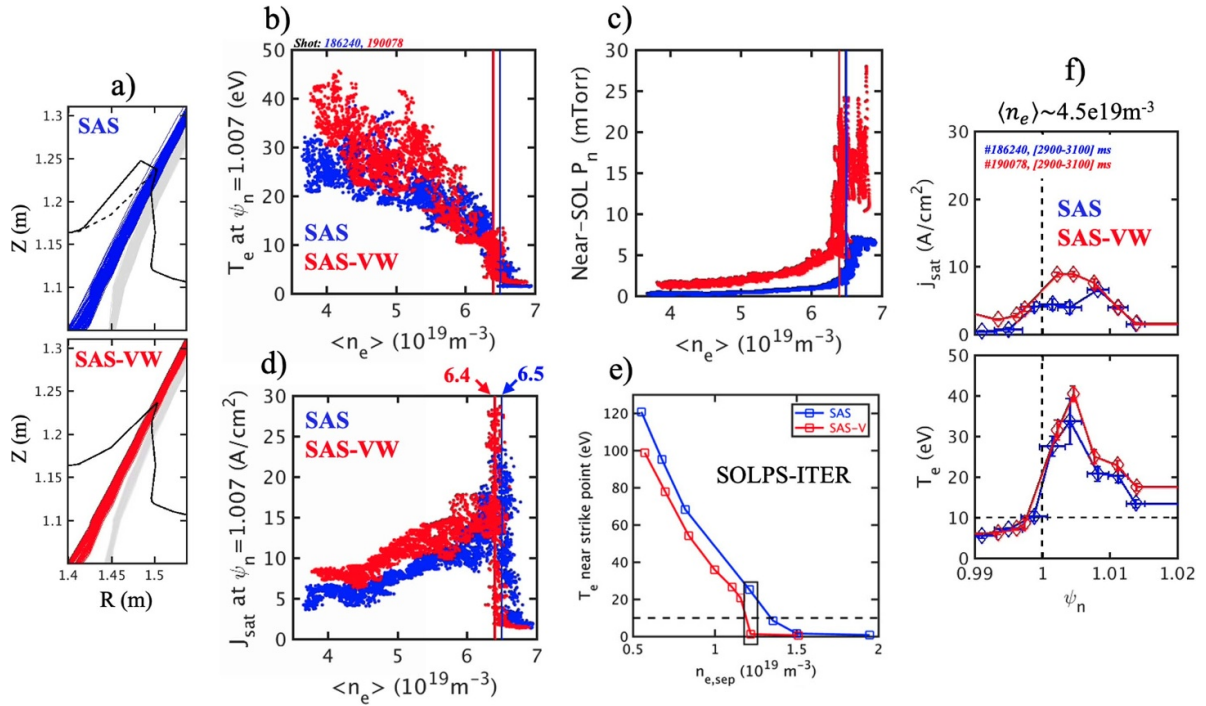


Figure 3. Effect of slot shape: flat-end SAS divertor (blue) compared to V-shaped SAS-VW divertor (red), for ion $\vec{B} \times \nabla B$ drift into the slot. In (b)–(d), vertical solid lines indicate the density corresponding to the rollover of the near-SOL J_{sat} and thus onset of divertor detachment. Sub-figure (e) is Reproduced from [20]. © 2021 IAEA, Vienna. All rights reserved, with the horizontal dashed line indicating $T_e = 10$ eV.

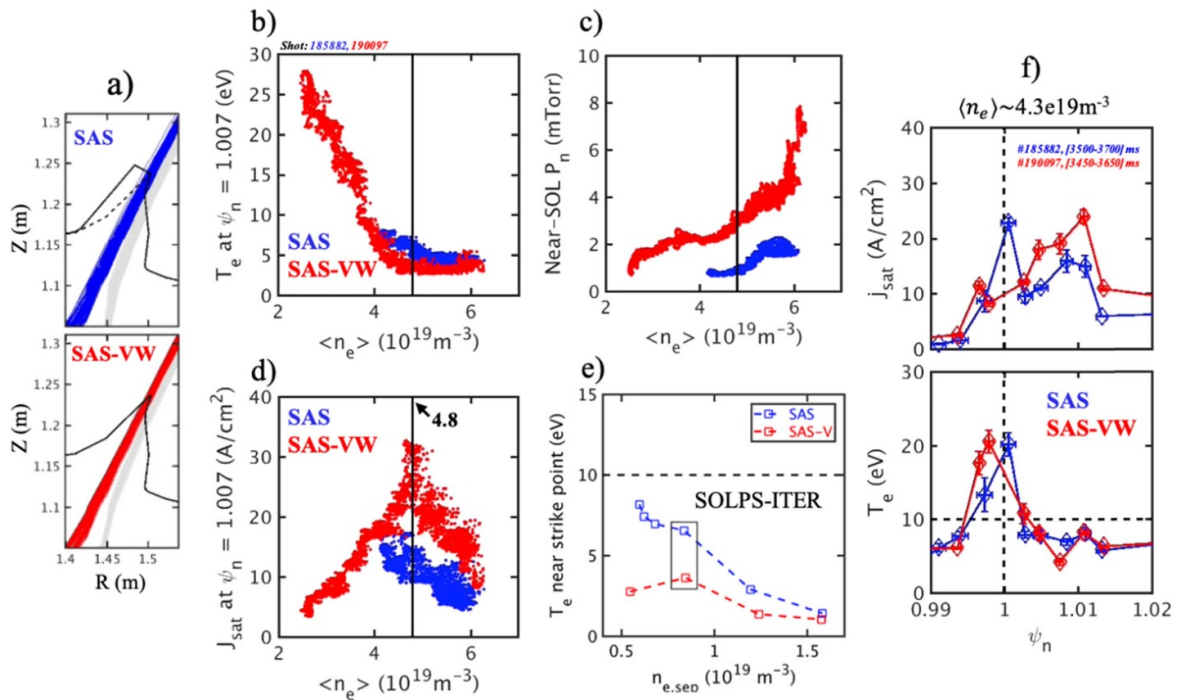


Figure 4. Effect of slot shape: flat-end SAS divertor (blue) compared to V-shaped SAS-VW divertor (red), for ion $\vec{B} \times \nabla B$ drift out of the slot. In (b)–(d), vertical black solid lines indicate the density corresponding to the rollover of the near-SOL J_{sat} and thus onset of divertor detachment. Sub-figure (e) is Reproduced from [20]. © 2021 IAEA, Vienna. All rights reserved. Note that the y-scales of sub-figures (b)–(f) are different from figure 3.

diagnostic measurements in the new slot divertor. Ultimately, simulations of SAS-V did not account for the presence of tungsten (sourced from the slot outboard tile). Although tungsten

might not radiate at such low divertor temperatures [21], and its source may not be significant (the W sputtering threshold is approximately 50 eV for carbon and 200 eV for deuterium

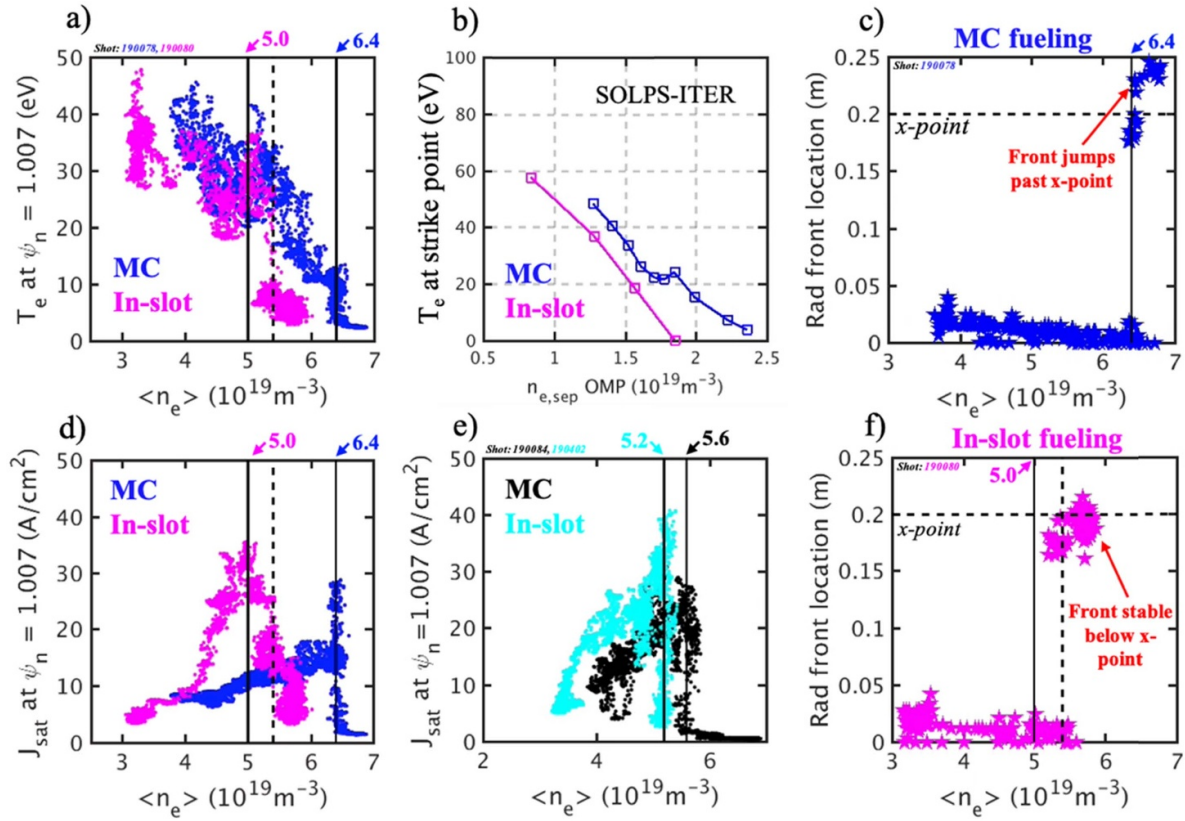


Figure 5. Effect of gas fuelling location: main chamber valve ('MC') compared to in-slot valve ('In-slot'), with ion $\vec{B} \times \nabla B$ drift into the slot and strike point at the slot vertex (a)–(b)–(c)–(d)–(f) or at the inner slant (e). (a)–(d)–(e) are from target Langmuir probes, (b) from SOLPS-ITER simulations and (c)–(f) from inversion of C-III line emission measurements by the DIII-D Tang TV camera [23]. Vertical black solid lines indicate the density corresponding to the rollover of the near-SOL J_{sat} and thus onset of divertor detachment.

[15]), its presence could still have some impact on divertor particle flows and, consequently, the overall divertor plasma solution.

3. Impact of in-slot fuelling on detachment onset

Detachment onset in the SAS-VW divertor is found to occur at lower upstream plasma density with in-slot gas fuelling (valve position shown in figure 2) compared to MC fuelling, as shown in figures 5(d) and (e) (without extrinsic impurities). Vertical black solid lines indicate the density corresponding to the rollover of the near-SOL ion saturation current and thus onset of divertor detachment. This reduction is $\sim 22\%$ for strike point on the vertex (from 6.4 to $5.0 \times 10^{19} \text{ m}^{-3}$, see figure 5(d)) and $\sim 7\%$ for strike point on the inner slant (from 5.6 to $5.2 \times 10^{19} \text{ m}^{-3}$, see figure 5(e)), with ion $\vec{B} \times \nabla B$ drift into the slot. The effect is captured by SOLPS-ITER simulations, showing a comparable $\sim 20\%$ reduction of the upstream separatrix density required to achieve 10 eV near the strike point with in-slot compared to main-chamber fuelling (figure 5(b)), and is consistent with the impact seen in SAS experiments [22]. The SOLPS-ITER simulations have 4 MW of injected power, uniform transport coefficients ($D = 0.15 \text{ m}^2 \text{ s}^{-1}$ and $\chi_e = \chi_i = 0.5 \text{ m}^2 \text{ s}^{-1}$) enhanced by 5 in the divertor and private flux region (PFR) regions beginning at the X-point elevation,

and neutral puff rates ranging from 4 to $14 \times 10^{21} \text{ D s}^{-1}$ with the MC valve and from 2 to $8 \times 10^{21} \text{ D s}^{-1}$ with the in-slot valve. The effect is less pronounced ($\sim 5\%$) with ion $\vec{B} \times \nabla B$ drift out of slot (not shown).

Fuelling from the in-slot valve also creates a delay between the sharp drop of target electron temperature, at $\langle n_e \rangle \sim 5.4 \times 10^{19} \text{ m}^{-3}$ (indicated by a vertical dashed line in figure 5(a)), and the roll-over of the ion saturation current, at $\langle n_e \rangle \sim 5.0 \times 10^{19} \text{ m}^{-3}$ (indicated by a vertical solid line in figure 5(d)). This is in contrast to the typical observation, when MC puffing is used in this drift direction, that the electron temperature drop and roll-over of ion current are simultaneous. Currently, the exact reason for this delay remains unclear, and this phenomenon is not reproduced by SOLPS-ITER simulations.

In addition, with ion $\vec{B} \times \nabla B$ drift into the slot, when the target is fully detached (after the J_{sat} rollover), the radiation front as indicated by visible C-III emission remains close to the X-point with in-slot fuelling (figure 5(f)), while it moves upstream of/beyond the X-point with MC fuelling (figure 5(c)). Movement of the radiation front upstream of the X-point is often associated with degradation of the plasma pedestal. In-slot gas fuelling has thus the potential to mitigate plasma pedestal degradation at divertor detachment, compared to MC gas fuelling, and can be a better way to develop a plasma core-edge integrated solution.

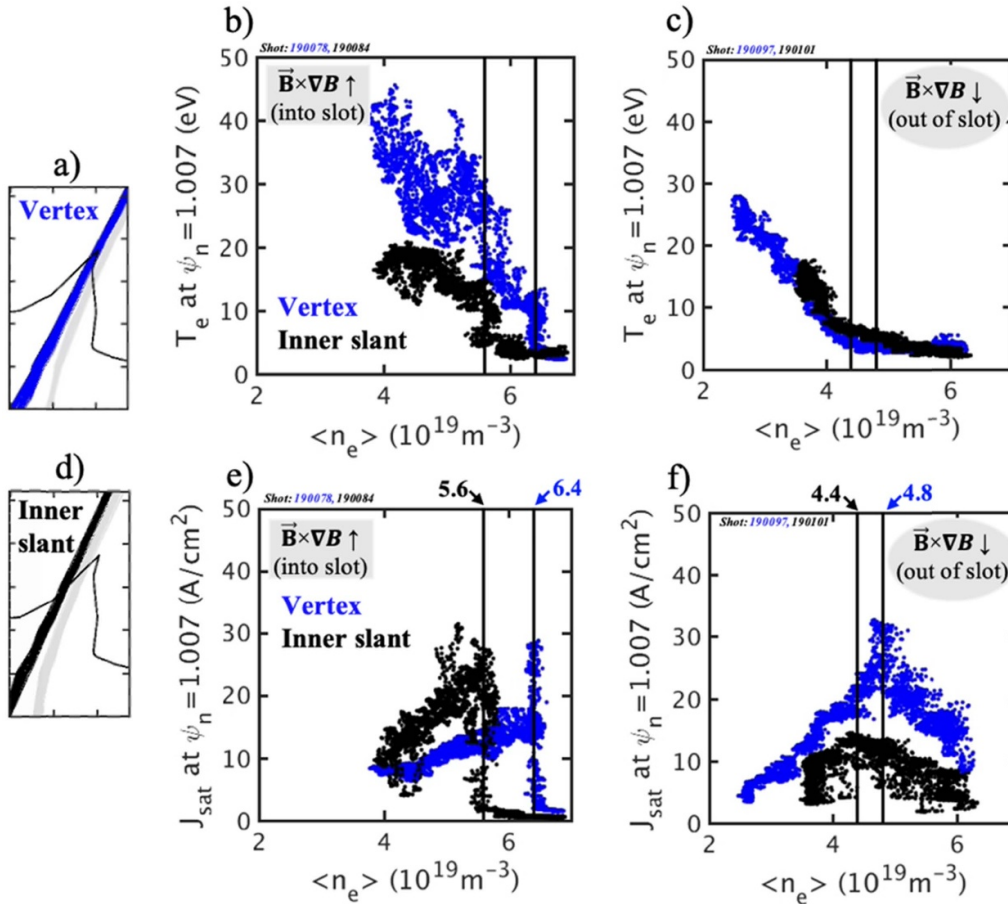


Figure 6. Langmuir probe data showing the effect of strike point position: at slot vertex (blue) compared to inner slant (black), for ion $\vec{B} \times \nabla B$ drift into (a)–(c) and out of (b)–(d) the divertor. (e)–(f) Reconstructed magnetic separatrix and strike point.

4. Impact of strike point position on detachment onset

Target plasma T_e is reduced when the outer strike point is placed on the inner slanted baffle compared to the slot V-end (figures 6(b) and (c)), in each B_T direction, such that detachment onset also occurs at lower upstream plasma density (without extrinsic impurities). Experiments were run with the strike point fixed at different locations in the SAS-VW slot (figures 6(a) and (d)), each with a density ramp using MC puffing to detachment onset and beyond. The reduction in detachment density is $\sim 12\%$ and $\sim 8\%$ for ion $\vec{B} \times \nabla B$ drift into (figure 6(e)) and out of the slot (figure 6(f)), respectively. This effect is consistent with multiple SAS experiments [22, 24, 25] and is observed for a range of plasma currents and heating powers (from separate DIII-D experiments, see [26]).

SOLPS-ITER simulations (not shown here but reported in [26]) with particle drift effects qualitatively reproduce the strike point position effect for ion $\vec{B} \times \nabla B$ drift into the divertor. Note that these simulations are based on plasma discharges from a separate experiment, running at higher plasma current and heating power ($I_P = 1.25$ MA and $P_{NBI} \sim 9$ MW compared to $I_P = 1$ MA and $P_{NBI} \sim 4$ to 5 MW for the cases in figure 5), and that no simulations are available for the opposite

drift direction. Transport coefficients are determined from the experiment as described in [20]. The simulations explain the inner slant benefit in terms of changes to $\vec{E} \times \vec{B}$ flows in the SOL. Specifically, the poloidal $\vec{E} \times \vec{B}$ flow in the near-SOL, directed towards the target for this drift direction, is ~ 10 times stronger if the strike point is on the inner slant compared to the vertex [26]. Since the flow direction is towards the plate, increased poloidal flow causes increased recycled neutral flux and thus a denser and colder plasma at the target. Ongoing analysis to identify the causes of this flux enhancement focuses on a potential positive feedback cycle involving slot geometry (target angles), radial temperature gradients, and radial electric field.

5. Impact of particle drift direction on detachment onset

The evolution from attached to detached conditions in SAS-VW strongly depends on the ion $\vec{B} \times \nabla B$ drift direction (see figure 7), in accord with experiments in SAS [11] and SOLPS-ITER simulations for SAS [12]. The comparison is done with the strike point fixed on the slot vertex (as in figure 6(a)) and a density ramp carried out using MC D₂ gas puffing. The drift

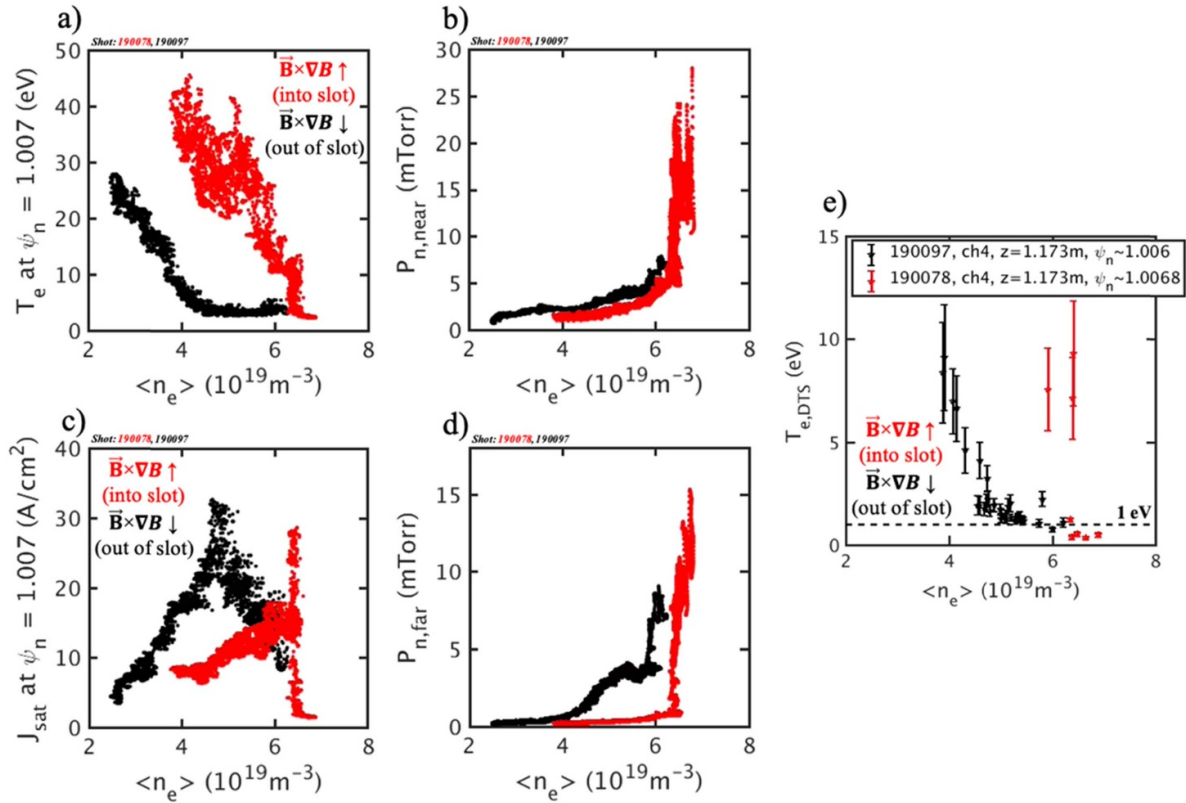


Figure 7. Effect of particle drift direction: ion $\vec{B} \times \nabla B$ drift into (red) and out of (black) the divertor. Figures (a)–(c) are from target Langmuir probes, (b)–(d) from target pressure gauges and (e) from divertor Thomson scattering. The plasma line-averaged density is increased using a valve in the main-chamber and the strike point is at the slot vertex.

direction is reversed by reversing the sign of the magnetic field.

For ion $\vec{B} \times \nabla B$ drift into the divertor, the divertor plasma sharply transitions from an attached to a detached state at a relatively high plasma density, with the electron temperature exhibiting a cliff-like drop from ~ 10 eV to ~ 1 eV as measured locally by DTS, figure 7(e) or ~ 5 eV as measured by surface LPs, figure 7(a). This sharp state transition is observed also in the SAS divertor [11] and in the open LSN divertor [27] and it is understood to be primarily driven by the interdependence of $\vec{E} \times \vec{B}$ -drift fluxes, divertor electric potential structure, and divertor conditions [28].

For ion $\vec{B} \times \nabla B$ drift out of the divertor, in contrast, the divertor smoothly transitions from attached to detached state as density rises but at a much lower plasma density value than the opposite drift direction, see figures 7(a)–(e). This is consistent with the change in the poloidal $\vec{E} \times \vec{B}$ drift direction which, for ion $\vec{B} \times \nabla B$ drift out of the divertor, drives particles from the PFR into the SOL across the separatrix, densifying and cooling the SOL plasma and thus facilitating detachment at low upstream plasma density.

The shape of target plasma profile properties (electron temperature, ion saturation current) is also found to depend

significantly on the ion $\vec{B} \times \nabla B$ direction. Data is shown for two nearly matched discharges with the outer strike point on the SAS-VW vertex and ion $\vec{B} \times \nabla B$ into (figures 8(a) and (b)) or out of (figures 8(c) and (d)) the divertor, with similar heating power (4 to 5 MW) and same plasma current (1 MA). When the $\vec{E} \times \vec{B}$ drift force removes particles from the PFR to the SOL (ion $\vec{B} \times \nabla B$ out of divertor), T_e is strongly reduced in the SOL such that the T_e profile peaks at the separatrix or even in the PFR (figure 8(d)), while it displays a more conventional peak in the SOL for the opposite drift direction (figure 8(b)). Magnetic field direction also affects the ion saturation current profile in detached conditions, which is flat for ion $\vec{B} \times \nabla B$ into the divertor (figure 8(b)) while it features two peaks for the opposite drift direction (figure 8(d)). This double peak feature is also observed in the target heat flux measured by the SETCs array. Past DIII-D experiments with plasma in the LSN configuration, outer strike point on the lower open divertor plate and same drift direction (ion $\vec{B} \times \nabla B$ drift out of divertor) showed a similar double peak structure in the particle flux profile at the outer divertor, interpreted as the effect of $\vec{E} \times \vec{B}$ drift flows [29]. Similarly to SAS-VW, the double peak did not appear for the opposite drift direction (ion $\vec{B} \times \nabla B$ into the divertor).

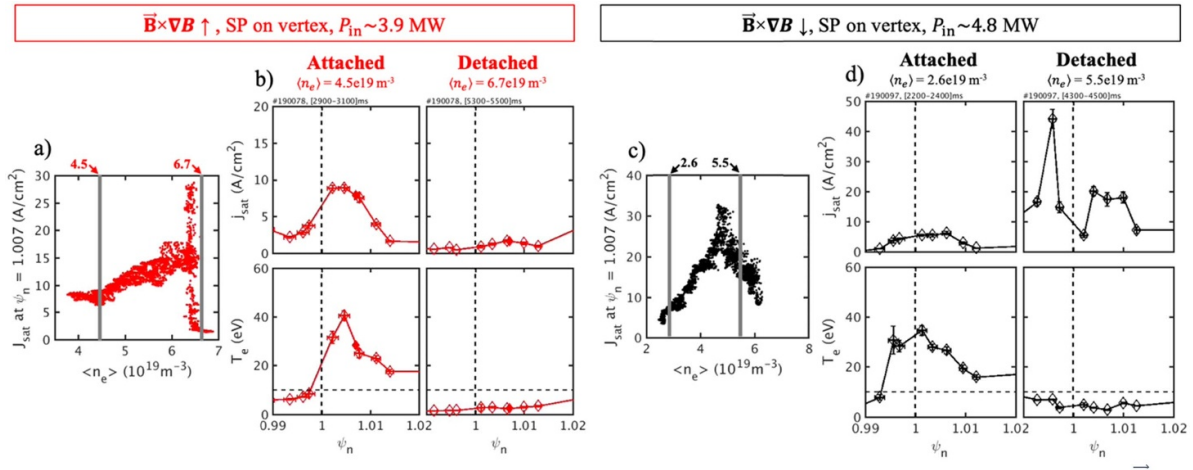


Figure 8. (a)–(c) Divertor target ion saturation current, in the near-SOL, as a function of plasma line-averaged density, with ion $\vec{B} \times \nabla B$ direction into (a) and out of (c) the divertor. (b)–(d) Target profiles of ion saturation current and electron temperature, as measured by Langmuir probes, in attached and detached conditions. Vertical grey lines in (a)–(c) indicate the density values corresponding to insets (b)–(d).

6. Discussion and conclusions

This set of DIII-D experiments demonstrate that the key power exhaust properties of a V-shape slot divertor (SAS-V) are essentially comparable to that of a flat-end slot divertor (SAS), with a very similar trajectory from attached to detached conditions. A flat-end and a V-shape slot divertor do, therefore, display the same power exhaust benefits relative to more open divertor configurations. From the engineering standpoint, the similarity in behaviour between SAS and SAS-VW has the positive implication that small (unavoidable) deviations in the slot manufactured shape from its nominal shape will not substantially change or compromise its capability to exhaust power. The similar behaviour observed in SAS-VW and SAS contrasts with SOLPS-ITER drift simulations, predicting a $\sim 10\%$ reduction in detachment density for SAS-VW compared to SAS. Possible explanations for this discrepancy include measurement uncertainty (scatter), imperfect toroidal slot symmetry, or the presence of tungsten, which is not modelled.

Practical ways to facilitate low density detachment in a slot divertor are experimentally identified. To minimize the plasma density for detachment, as necessary for core plasma scenarios at low collisionality, the strike point should be placed on the inner slanted baffle (instead of the slot end) and/or fuelling gas should be injected from an in-slot valve (instead of from the main-chamber). SOLPS-ITER modelling, with drift effects included, captures the strike point position effect in terms of a change of the particle drift flows in the slot, and the valve position effect in terms of a change in the divertor neutral retention and (thus) divertor radiation. The data also shows that a plasma core-edge integrated solution may be

easier to develop by fuelling neutral gas from the slot (instead of from the main-chamber), though a thorough analysis of pedestal plasma profiles is necessary before drawing definitive conclusions about changes in core-edge integration. These experiments represent an additional example of validation of the SOLPS-ITER model and demonstrate that accounting for $\vec{E} \times \vec{B}$ drifts is essential to understand particle and power dynamics in tight divertor structures. This is particularly relevant to future fusion devices operated at low upstream density, where access to detachment is critical to maintain divertor armour integrity.

Currently, a clean extrapolation of these findings to a fusion pilot plant (FPP) is not straightforward, because the divertors within an FPP are anticipated to incorporate pumping systems to regulate impurities and plasma density, in contrast to SAS and SAS-VW, and will operate at much higher plasma density and target heat fluxes. However, the upcoming DIII-D staged divertor program will present a unique opportunity to characterize the detachment performance of tightly baffled (closed) divertors with active pumping and in more reactor-relevant conditions. This will subsequently bolster confidence in extrapolating these findings to an FPP.

The design of future divertors is also informed by these results. The clear benefit of placing the strike point on the inner slant—a shift of only a few centimetres for the scale lengths of the plasma profile in the SAS slot—and that of using in-slot gas fuelling mean that future divertors (and coil systems) should be designed in a way that the strike point can be moved and placed onto an inboard slanted surface, and should feature in-slot fuelling valves (for deuterium and low-Z radiating impurities) in addition to conventional main-chamber valves.

Acknowledgments

This material is based upon work supported by the US Department of Energy, Office of Science, Office of Fusion Energy Sciences, using the DIII-D National Fusion Facility, a DOE Office of Science user facility, under Award(s) DE-FC02-04ER54698, DE-AC05-00OR22725, DE-AC52-07NA27344, DE-SC0023378 and DE-NA0003525.

Disclaimer

This report was prepared as an account of work sponsored by an agency of the United States Government. Neither the United States Government nor any agency thereof, nor any of their employees, makes any warranty, express or implied, or assumes any legal liability or responsibility for the accuracy, completeness, or usefulness of any information, apparatus, product, or process disclosed, or represents that its use would not infringe privately owned rights. Reference herein to any specific commercial product, process, or service by trade name, trademark, manufacturer, or otherwise does not necessarily constitute or imply its endorsement, recommendation, or favouring by the United States Government or any agency thereof. The views and opinions of authors expressed herein do not necessarily state or reflect those of the United States Government or any agency thereof.

ORCID iDs

R. Maurizio  <https://orcid.org/0000-0001-9896-6732>
 D. Thomas  <https://orcid.org/0000-0002-1217-7773>
 J.H. Yu  <https://orcid.org/0000-0003-0833-5131>
 T. Abrams  <https://orcid.org/0000-0002-9605-6871>
 A.W. Hyatt  <https://orcid.org/0000-0003-3384-5280>
 J. Herfindal  <https://orcid.org/0000-0003-2846-597X>
 A. Leonard  <https://orcid.org/0000-0001-9356-1074>
 X. Ma  <https://orcid.org/0000-0002-7326-2146>
 A.G. McLean  <https://orcid.org/0000-0002-0697-4397>
 J. Ren  <https://orcid.org/0000-0002-2256-1007>
 F. Scotti  <https://orcid.org/0000-0002-0196-9919>

M.W. Shafer  <https://orcid.org/0000-0001-9808-6305>
 G. Sinclair  <https://orcid.org/0000-0003-4195-177X>
 H.Q. Wang  <https://orcid.org/0000-0003-1920-2799>

References

- [1] Stangeby P. and Leonard A.W. 2011 *Nucl. Fusion* **51** 063001
- [2] Stangeby P. 2018 *Plasma Phys. Control. Fusion* **60** 044022
- [3] Kallenbach A. et al 2015 *Nucl. Fusion* **55** 053026
- [4] Leonard A., Makowski M.A., McLean A.G., Osborne T.H. and Snyder P.B. 2015 *J. Nucl. Mater.* **463** 519
- [5] Ishida S. et al 1997 *Phys. Rev. Lett.* **79** 3917
- [6] Bernert M. et al 2017 *Nucl. Mater. Energy* **12** 111
- [7] Wang H. et al 2021 *Phys. Plasmas* **28** 052507
- [8] Loarte A. 2001 *Plasma Phys. Control. Fusion* **43** R183–24
- [9] Reimerdes H. et al 2022 *Nucl. Fusion* **62** 042018
- [10] Verhaegh K. 2023 *Nucl. Fusion* **63** 016014
- [11] Guo H. et al 2019 *Nucl. Fusion* **59** 086054
- [12] Ma X., Wang H.Q., Guo H.Y., Stangeby P.C., Meier E.T., Shafer M.W. and Thomas D.M. 2021 *Nucl. Fusion* **61** 054002
- [13] Ma X. et al 2022 *Nucl. Fusion* **62** 126048
- [14] Abrams T. et al 2021 *Phys. Scr.* **96** 124073
- [15] Brezinsek S. et al 2019 *Nucl. Fusion* **59** 096035
- [16] Parsons M. et al 2023 *Nucl. Mater. Energy* **37** 101520
- [17] Messer S.H. 2024 *Nucl. Mater. Energy* **38** 101566
- [18] Brooks J.N., Sizyuk T., Sinclair G. and Hassanein A. 2021 *Nucl. Fusion* **61** 126071
- [19] Du H., Guo H.Y., Stangeby P.C., Bonnin X., Zheng G., Duan X. and Xu M. 2020 *Nucl. Fusion* **60** 126030
- [20] Maurizio R. et al 2021 *Nucl. Fusion* **61** 116042
- [21] Putterich T., Fable E., Dux R., O'Mullane M., Neu R. and Siccino M. 2019 *Nucl. Fusion* **59** 056013
- [22] Wang H. et al 2022 *Nucl. Mater. Energy* **33** 101301
- [23] Fenstermacher M. 1997 *Rev. Sci. Instrum.* **68** 974–7
- [24] Casali L., Osborne T.H., Grierson B.A., McLean A.G., Meier E.T., Ren J., Shafer M.W., Wang H. and Watkins J.G. 2020 *Phys. Plasmas* **27** 062506
- [25] Shafer M. et al 2019 *Nucl. Mater. Energy* **19** 487–92
- [26] Thomas D. 2023 Milestone 2023–2: mitigate ExB effects in SAS by modest change of tile shape to improve power mitigation for both Bt directions *Milestone Report for DOE*
- [27] McLean A.G. et al 2015 *J. Nucl. Mater.* **463** 533–6
- [28] Jaervinen A. et al 2018 *Phys. Rev. Lett.* **121** 075001
- [29] Wang H., Watkins J.G., Guo H.Y., Groth M., Jarvinen A.E., Leonard A.W., Ren J., Thomas D.M. and Boedo J. 2021 *Phys. Plasmas* **28** 052509